ALMA Memo No. 488
Wide-Field Imaging of ALMA with the Atacama Compact Array: Imaging Simulations

Takahiro Tsutsumi[1], Koh-Ichiro Morita[2], Tetsuo Hasegawa[1],
and
Jérôme Pety[3,4]

[1] *National Astronomical Observatory of Japan (NAO-J), 2-21-1 Osawa, Mitaka, Tokyo 181-8588, Japan*
tsutsumi@alma.mtk.nao.ac.jp, tetsuo.hasegawa@nao.ac.jp
[2] *Nobeyama Radio Observatory, NAO-J, Nobeyama, Minamimaki, Minamisaku, Nagano 384-1305, Japan*
morita@nro.nao.ac.jp
[3] *IRAM, 300 rue de la Piscine, 38406 Grenoble Cedex, France*
pety@iram.fr
[4] *LERMA, Obs. de Paris*

March 21, 2004

Abstract

We examined the significance of the Atacama Compact Array (ACA) in wide-field imaging of ALMA through imaging simulations. The purpose of the simulations are to i) demonstrate importance of ACA in wide-field imaging with ALMA and ii) identify which component of errors has more significant influence than others on quality of final images obtained with ALMA+ACA using realistic parameters as to give feedback on designing and specifications of the ACA system. We particularly focused on the following aspects: difference on the ACA configuration design and effects of pointing errors, amplitude errors, and atmospheric phase errors. The simulations indicate that how densely packed the ACA configuration is an important factor for good imaging performance. The pointing errors at submm waves seriously degrade fidelity of an image. The atmospheric phase fluctuation also plays a major role. As indicated by previous works, our study indicates that ACA can boost the quality of wide-field imaging with ALMA by a factor of two or more for many cases, while dependency on structures of model images exists. In presence of all the errors, the projected goal of the imaging fidelity of 20 or better for ALMA when ACA is included, can be achieved if the current specifications are met.

1 Introduction

The Atacama Compact Array (ACA) system which is being proposed by Japan to use jointly with the ALMA 64-element array to enhance the wide-field imaging capability of ALMA. The ACA system consists of an array with twelve 7-m antennas in closely packed configuration and four 12-m antennas as single dishes for total power measurement and calibration. ACA recovers the shorter baseline information that is missing from the data taken by the ALMA 64-element array alone by directly sampling short uv-spacing. As the field of view for the ALMA 12m 64-element array, which is $18''$ at 345 GHz and $7''$ at 850 GHz, are relatively small, it is anticipated that wide-field imaging by mosaic has a large demand in scientific observations using ALMA, particularly at sub-millimeter wavelengths. In the recent report of the ALMA Design Reference Science Plan (DRSP) of Version 1

(van Dishoeck, Wootten, & Guilloteau 2003), the scientific projects that proposed to include ACA amount to about 41 % of total hours requested in the DRSP.

The homogeneous 64-element array alone is not sufficient to produce high quality mosaic images. However, high fidelity wide-field imaging with ALMA will be made possible by adding the ACA system with its smaller high precision antennas providing short spacing information as well as its dedicated single-dish telescopes for zero spacing information.

Several imaging simulation studies for the impact of ACA in the wide-field imaging capability of ALMA have been conducted. Yun (2001) and Morita (2001) used maximum entropy methods for deconvolution of a mosaic image. The basic ACA configuration was studied by Yun and further analysis including pointing error effect were conducted by Morita. Pety, Gueth and Guilloteau (2001a, 2001b, 2001c) using CLEAN-based deconvolution for mosaicing, investigated imaging capability of ACA under various errors. All the authors concluded the importance of the ACA system in high quality wide-field imaging.

As the detailed design of ACA is taking shapes now, it is very important to re-investigate these simulations to test specific parameters and reflect these results in the design of the ACA system. For our simulations, we adopted tools used by Pety et al and following similar paths as they did. In this memo, we report our investigation of two important aspects which might influence imaging quality: array characteristics (configuration, a ratio of close packing, etc) and the imaging capability under various errors. For the later, we studied the effects of pointing, amplitude, and atmospheric phase errors. We focused on imaging performance in realistic error conditions so as to give feedback in determination of optimal error budget for the system.

2 Simulation Procedures

We used the GILDAS ALMA+ACA simulation tools for our investigation. The simulator was developed in the GILDAS data reduction software environment by the IRAM group (Pety et al. 2001a, 2001b, 2001c) to study wide-field imaging performance of ALMA by adding the ACA observations to the ALMA 64-element array observations. For detailed description of the simulator, one should refer to Pety et al (2001c). Here we describe the basic procedures of the simulator.

The simulator simulates observing sequences and generates the simulated visibility data for the 64-element and ACA arrays (In this memo, we often referred the 7-m array of ACA as ACAi) based on given input parameters. For single dish (SD) data, a pointed observation at the center of each field is simulated when it is combined with the 64-element array visibilities to produce ALMA+SD data. The on-the-fly mapping is simulated to derive short spacing information up to the distance of 5m (difference in the dish diameters of the SD and ACAi element) in uv-plane when it is combined with ACAi visibilities to produce ACAi+SD data. Using these data, the mosaic dirty images are created. In the GILDAS simulator, two types of imaging method for the heterogeneous array are provided. In the uv-plane hybridization method, the ALMA+SD and ACAi+SD images are separately created and deconvolved. Then the two images are Fourier transformed to uv domain and linearly combined in the uv-plane, then the combined visibility data are transformed back to the image. The other method is a CLEAN-based joint-deconvolution method which simultaneously use the ALMA and ACA dirty mosaic-ed images in the CLEAN process to generate a single combined image. In our simulations, the joint-deconvolution method occasionally gave unreasonable results, which may require more fine tuning of the parameters. Therefore, for our current purpose, we adopted the hybrid method which is more straight forward and gives more uniform reliable results than the true-joint deconvolution method. This also significantly reduces CPU time for simulations. The GILDAS with the ALMA simulator tools was installed on the Intel Pentium 4 and dual CPU Xeon based PCs running RedHat Linux. Nearly two thousand sets of simulations were performed.

2.1 Simulation parameters

Some of common parameters used in the simulation results presented here are summarized in Table 1. For the simulations to study the influence of the ACA configuration characteristics without errors (Section 3), 230 GHz is used as an observing frequency. For the simulations including errors (Section 4), two observing frequencies, 230 and 850 GHz, are considered. We assume durations of observations to be relatively short with the hour angle ranges of ± 0.15 hr and ± 0.6 hr for the 64-element array and ACAi, respectively. For the 64-element array, the most compact configuration, C1 is used. The configuration data currently available to us is based on 60 elements. Thus we adopt this data to represent the 64-element configuration.

The number of fields for mosaic is 19. We found that higher image fidelity was obtained for 19-field mosaics than for the 7-field ones as were used by Pety et al (2001c) (typically, the fidelity increases by 10-20%). We used four model images (M51Hα, M31, cluster, HCO$^+$(4-3)) as used in Pety et al. Figure 1 and 2 list models scaled for the 230 GHz case ($70'' \times 70''$) in image- and uv-planes. For all the model images, the declination of -23 degree is used. As we stated earlier, uv-plane hybridization method is used for mosaic imaging for the ALMA+ACA data. The deconvolved ALMA+SD and ACAi+SD images are combined in the uv domain by selecting the ACA data up to a transition radius and the ALMA data for longer uv distances than the transition radius (an exponential function is used to ensure smooth transition around the transition radius). The transition radius is set to 15 m as the uv response of ACA quickly diminishes beyond this distance (Morita & Holdaway 2004).

Array configuration of ALMA 64-element array	c1	
no. mosaic field	19	
Observing frequency	230GHz	850GHz
image size	$70''$x$70''$(230GHz)	$19''$x$19''$(850GHz)
model	M51Hα, cluster, M31, HCO43(HCO$^+$(4-3))	
source declination	-23 deg.	
observing hour angle range [hr]	ALMA -0.15 to 0.15; ACA -0.6 to 0.6	

Table 1: Common parameters

(a) M51Hα: image

(b) M51Hα: uv distribution

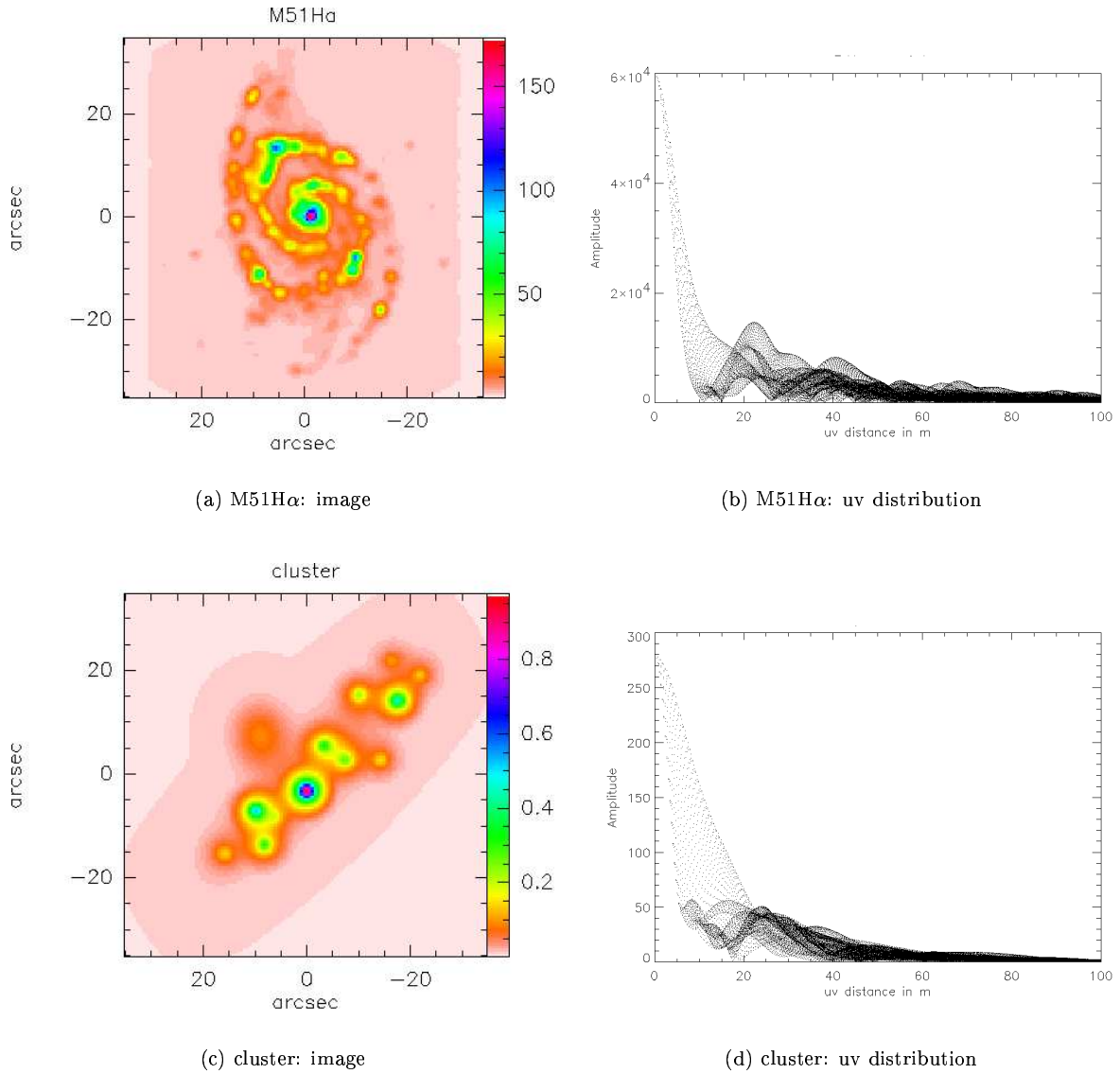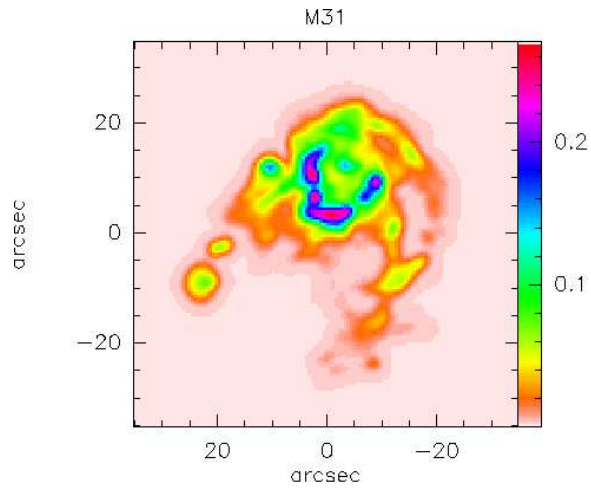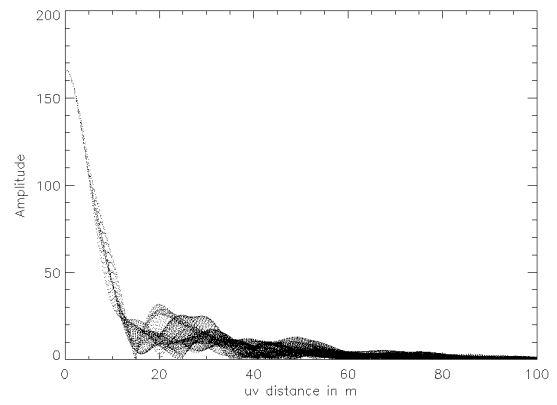
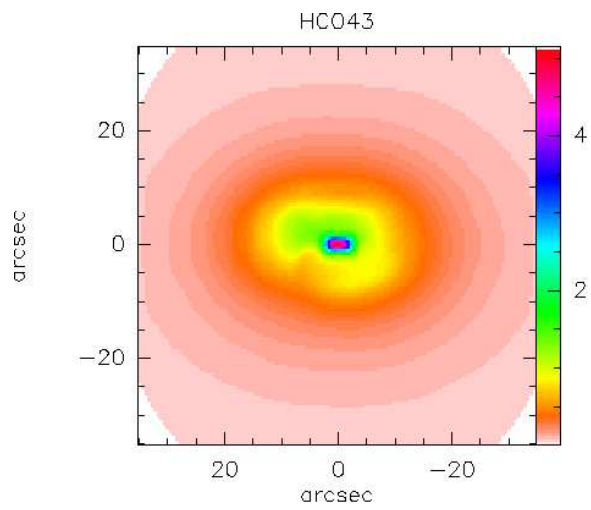(c) cluster: image

(d) cluster: uv distribution

Figure 1: Input models (at 230 GHz). The images are smoothed with the ALMA beam. In the *uv* distribution plots, only the data with the uv distance < 100m are shown.
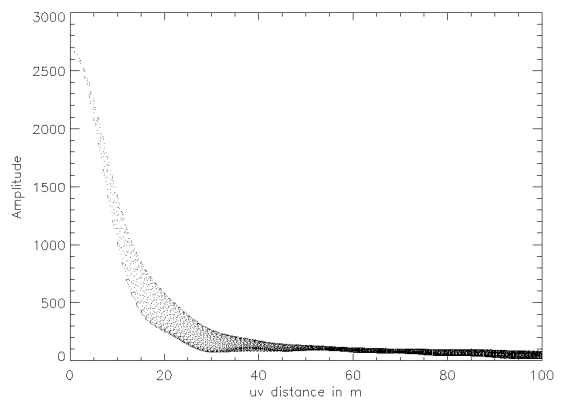
(a) M31: image

(b) M31: uv distribution

(c) HCO43: image

(d) HCO43: uv distribution

Figure 2: Input Models (continued)

2.2 Analysis

In the GILDAS simulator, a primary indicator to assess the quality of simulated images is fidelity. The image fidelity is computed at each pixel on the image following its definition (Pety et al 2001c):

$$Fidelity(i,j) = \frac{abs(Model(i,j))}{abs(Model(i,j) - Simulated(i,j))} \tag{1}$$

Actual calculations of fidelity in the simulator involve exclusion of the extremely high fidelity points (Eqn. 4. in Pety et al) to ensure that the determined fidelities reflect mean image quality. The median image fidelities at the four different pixel intensity cutoff (0.3, 1, 3, 10% of the peak intensity of the original image) are computed from the fidelity map. Also, the fidelity in the uv plane is obtained. The model and difference images are Fourier-transformed to the uv domain and then the uv fidelities are computed by dividing the model by the difference. The median fidelities at the four levels of uv range (0-15m, 15-37.5m, 37.5-75m, 75-150m) are evaluated.

3 Effects of ACA Array Configuration Characteristics on Imaging

Here we study the effects of different ACA configurations in imaging performance. Types of the array configuration for 12 7-m element ACA array used in these simulations are as shown in Figure 3. The configuration labeled as 'iram' is the one used by Pety et al (2001c) in their simulations and is generated randomly. The one labeled as 'mw2003' is from Wright (2003), which is generated by two nested Reuleaux triangles with optimizations using the code developed by Boone (2001). No optimizations were performed for the other two configurations that we generated. The observing frequency of 230 GHz is assumed for this part of simulations. The simulations were performed without errors.

3.1 Configuration Types

The four types of the configuration for ACA array are compared for the image fidelity in Table2. It lists the median image fidelity determined from the pixels with their intensity above the threshold value given in percentage of peak intensity of original images.

It is clear that the addition of ACA array greatly improves the imaging performance in general except for M31. The ratio of fidelities of ALMA+ACAi+SD over those of ALMA+SD (hereinafter referred as "fidelity gain") is typically 2 or greater for the other three models. Difference among the four types of configurations depends on source structure. For the M51Hα and HCO43 models, the ring performs poorly while for the rest of the configurations, the difference is not significant. Now, if we focus on the results for the fidelity medians that determined with the intensity threshold of 1% of peak intensity, the iram and spiral types have good overall performance for all the models.
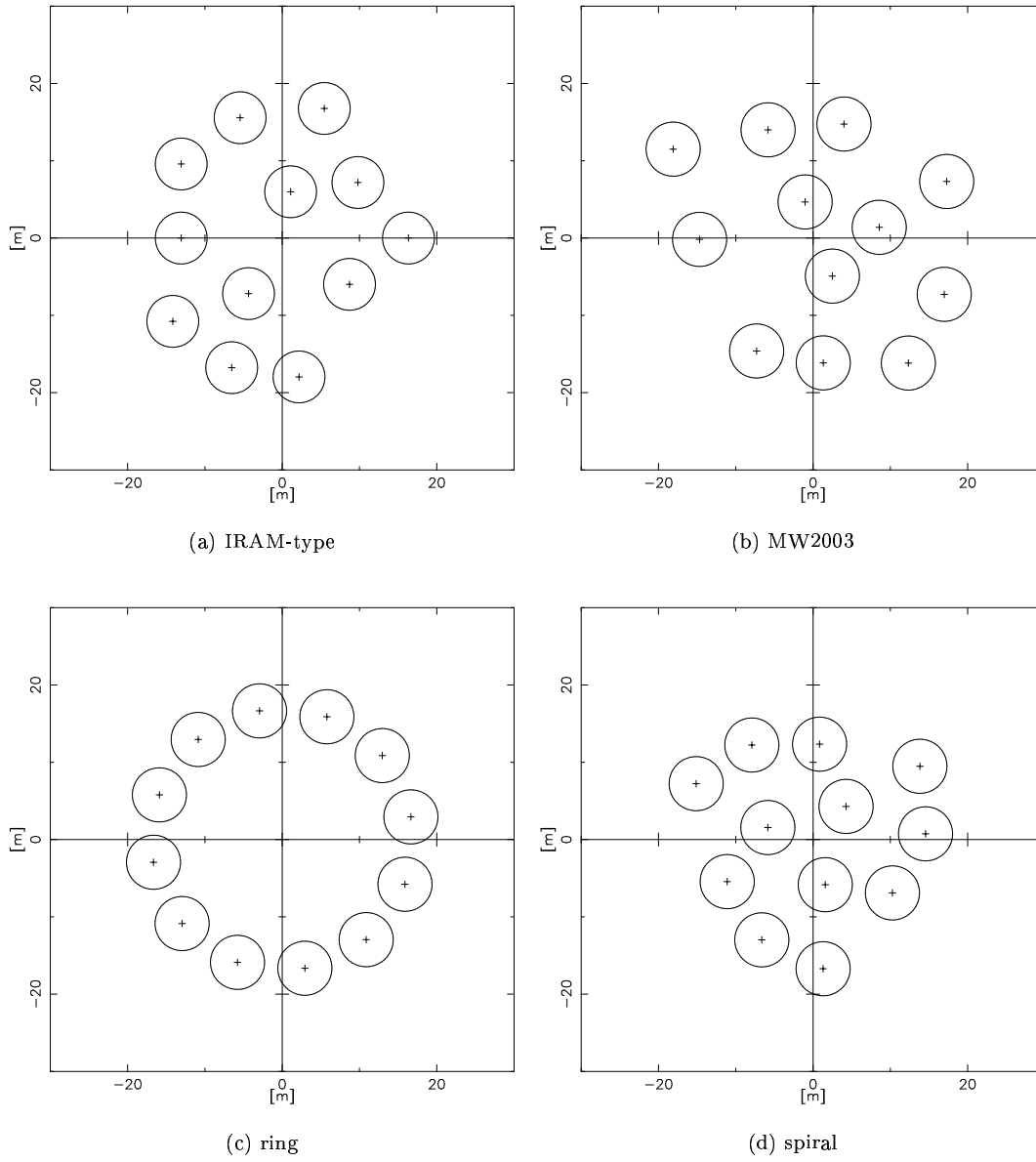
(a) IRAM-type

(b) MW2003

(c) ring

(d) spiral

Figure 3: ACA configuration types tested. All the configurations shown here are set to have a close packing ratio of 1.25.

model	ACA config.	Intensity threshold											
		0.30%			1%			3%			10%		
		ALMA+SD	all	fidelity gain	ALMA+SD	all	fidelity gain	ALMA+SD	all	fidelity gain	ALMA+SD	all	fidelity gain
HCO43	iram	6	66	10.9	8	110	14.6	21	156	7.3	20	168	8.3
	ring	6	13	2.1	8	17	2.3	21	42	2.0	20	52	2.6
	spiral	6	62	10.1	8	105	14.0	21	164	7.6	20	180	8.9
	mw2003	6	44	7.3	8	73	9.7	21	107	5.0	20	113	5.6
M51Hα	iram	5	54	11.0	28	148	5.3	51	206	4.0	102	300	2.9
	ring	5	15	3.0	28	44	1.6	51	85	1.7	102	180	1.8
	spiral	5	53	10.8	28	151	5.4	51	213	4.2	102	296	2.9
	mw2003	5	53	10.8	28	127	4.5	51	171	3.4	102	269	2.6
cluster	iram	46	195	4.3	65	250	3.9	95	300	3.2	186	408	2.2
	ring	46	161	3.5	65	224	3.5	95	292	3.1	186	403	2.2
	spiral	46	207	4.5	65	267	4.1	95	311	3.3	186	416	2.2
	mw2003	46	186	4.1	65	235	3.6	95	285	3.0	186	379	2.0
M31	iram	85	184	2.2	99	221	2.2	117	273	2.3	138	338	2.5
	ring	85	180	2.1	99	219	2.2	117	264	2.3	138	333	2.4
	spiral	85	184	2.2	99	220	2.2	117	278	2.4	138	331	2.4
	mw2003	85	183	2.2	99	221	2.2	117	276	2.4	138	333	2.4

Table 2: Comparison of median image fidelities with different ACA configurations (close packing ratio = 1.25), 19-field mosaic, no error case. ALMA+SD= ALMA 64 element array + single-dish, all= the 64-elment array with the ACA system using the hybrid method. The fidelity gain is defined as $\frac{all}{ALMA+SD}$.

These differences may be attributed to how compactly packed the array is. Figure 4 shows that the image median fidelity is in fact correlated with the number of visibility within the *uv* distance of 15m for the different type of the ACA array configuration. In comparison with sidelobes of the four types of the ACA configuration, the spiral and iram-types have lower rms sidelobe levels which are evaluated within a radius of three times the beam size. Figure 5 shows that comparison between the fidelities and sidelobe levels of the ACA beams.
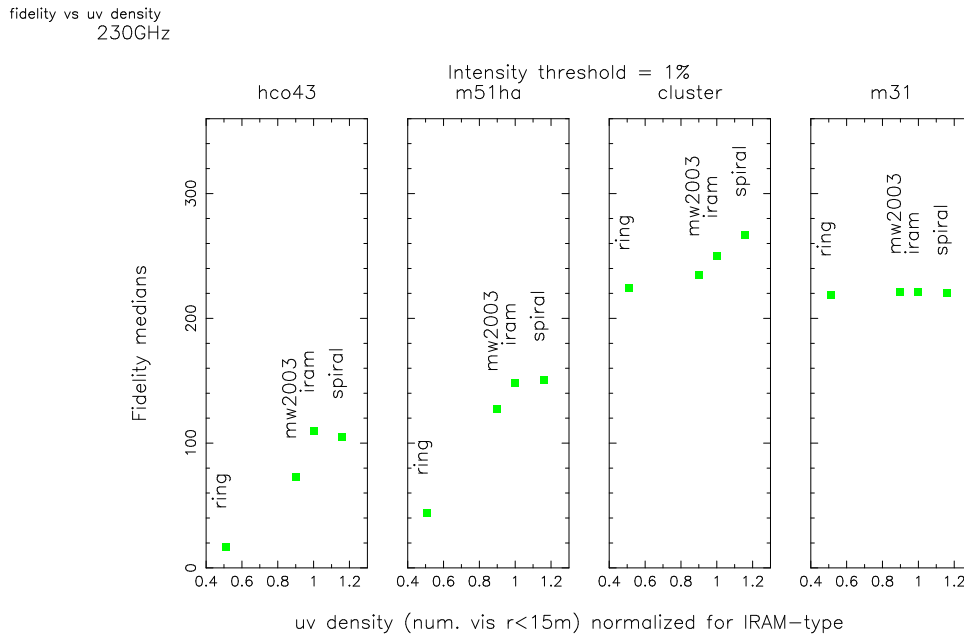

Figure 4: Relationship between image fidelity and the number of visibility within *uv* distance of 15m. The uv density were normalized to that of the iram-type configuration.

9

Intensity threshold = 1%

hco43   m51ha   cluster   m31

Fidelity medians

spiral
iram
mw2003

ring

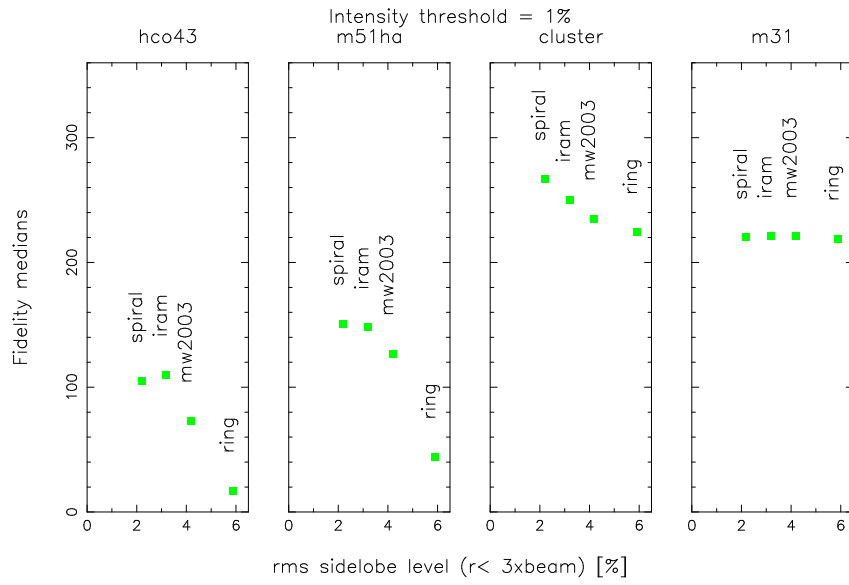rms sidelobe level (r< 3xbeam) [%]

Figure 5: Relationship between image fidelity and the rms sidelobe levels inside a radius of 3 x ACA beam.

3.2 Close Packing

We also examined the dependency of fidelity on ratios of close packing (minimum baseline/antenna diameter). The ACA configurations with different close packing ratios are generated by scaling a given configuration type. Figure 6 shows that uv fidelity medians in the uv range of 0-15m as the close packing ratio are varied between 1.15 to 1.35 for a spiral configuration. The fidelities in this uv range are essentially contribution from the ACAi+SD data. The red lines indicate the fidelities of ALMA+SD only. In all models, the smaller close packing ratio results in higher image fidelity. For the HCO43 and M51Hα models, the fidelity medians decline sharply for the close packing ratio greater than 1.30. Since the array is scaled as whole, the observed dependency is not only caused by variation in minimum baseline but also it is related to how densely packed.
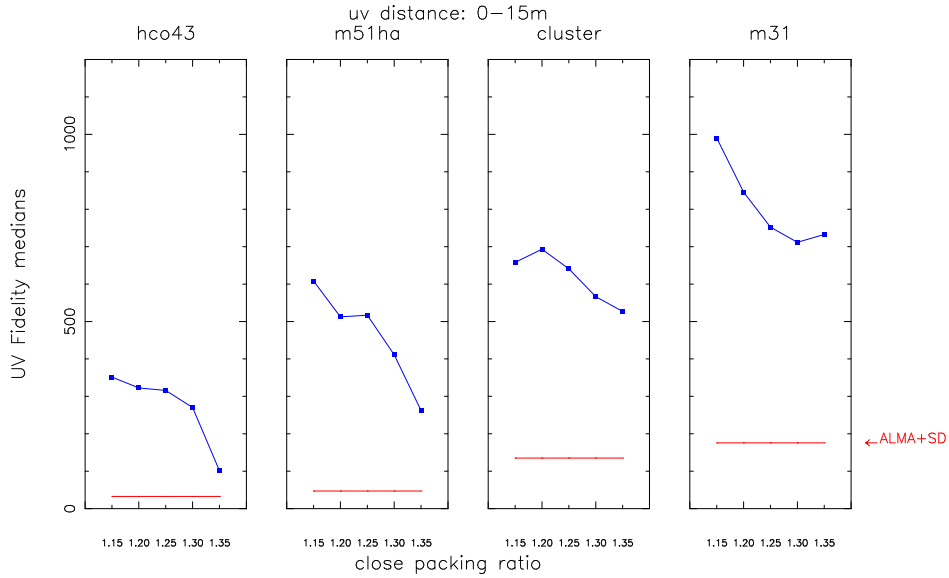

Figure 6: Comparison of fidelities in different close packing ratio of the spiral-type ACA configuration. ALMA+ACAi+SD cases are shown in blue lines. For reference, the fidelities of ALMA+SD cases are indicated in red lines.

3.3 Summary of Sec.3

We examined different array configuration characteristics. The number of visibility within certain uv radius (in this study, r_{uv}=15m) and close packing ratio are related to how the array is densely packed, or *compactness* of the array. While there are some variations among the source models, it is generally true that an array with higher degree of compactness (higher concentration of elements

toward the array center and the higher close packing ratio) gives better imaging performance.

One word of caution is that for the results presented above we used the most compact configuration (C1) for the 64-element array. Thus the *uv* response of the 64-element array extends short-ward of uv distances and the "*uv* gap" in the visibilities of the 64-element array filled by those of ACA is least. In actual operations, the 64-element array will be in C1 only in a relatively brief duration in the whole configuration cycle of the 64-element array and the ACA data is anticipated to combine with the data taken with the 64-element array in continuous reconfiguration, probably, up to an 1-km array. The contribution of ACA in such cases would be greater since sampling of spatial frequency <30m would be predominantly from ACA. In such cases, the compactness of the ACA array investigated here may not apply, or at least, the criteria of compactness could be different. Simulations with ALMA 64-element array's sparser configurations are needed before an optimal design of ACA array configuration is decided.

4   Simulations Including Systematic Errors

An investigation on which error has more influence on quality of final images obtained with the ALMA+ACAi+SD mode than others is important since it will, in turn, give feedback on the design of the ACA system. By addressing error budget that influence image quality of ALMA+ACA, it can help shape optimal designs to bring the most out of the ACA system. We consider here pointing, amplitude gain, and atmospheric phase errors.

For the simulation results reported in this section, a spiral-type with a close packing ratio of 1.25 was used for the ACA configuration. To represent both millimeter and submillimeter wavelengths condition, two observing frequencies, 230 and 850 GHz were used. Common parameters listed in Table 1 of Section 2 were used again for the simulations presented in this section.

For the rest of discussions in this section, we focus on the median fidelities determined from pixels with the intensity greater or equal to 1% of the peak intensity in the original image assuming that these represent average behaviors of imaging quality.

Treatments of various errors in the simulator are described in Pety et al (2001c). We give some comments on how we made particular choices of models of errors for our simulations in the following sections of individual errors. Some relevant ALMA 64-element array and ACA specifications which we make comparison with are listed in Table 3.

Pointing errors (offset) (ALMA&ACA)	$0.6''$
Close packing ratio of ACA	1.25
Amplitude error (ALMA& ACA)	1% for $\nu < 300$ GHz, 3% for $\nu > 300$ GHz

Table 3: ALMA specifications

4.1   Pointing Errors

In high fidelity wide-field imaging, good pointing accuracy is critical as pointed out by Cornwell, Holdaway, & Uson (1993) and Holdaway (1997). Pety et al (2001c) and Morita (2001) showed that the addition of ACA improves the situation.

The pointing errors are assumed to be residual random offsets per antenna after pointing calibration and set independently for each elements of the 64-element and ACA arrays and single dish (SD). More sophisticated models considering time variable wind- and thermally- induced effects were done by Pety et al (2001c). We assumed that systematic errors including the thermally induced effect can be corrected by calibration. The wind-induced pointing errors are randomly varying with short time scale and some coupling among antennas are expected. The effect can also be different between

the ACA 7-m and ALMA 12-m antennas under different observing parameters and conditions (i.e. observing frequency, observation by night or daytime, etc.) and they add more parameter space to explore for simulations. Therefore for our purpose, only random errors is considered assuming that the net effect in the image fidelity is reasonably represented with these errors. Note that as we described in Section 2, the single dish data for ALMA+SD and ALMA+ACAi+SD are treated differently. The former is from pointed observations and later is from on-the-fly mapping. Therefore, it could produce systematic difference between ALMA+SD and ALMA+ACAi+SD in the effect of pointing errors.

The ALMA specification for a pointing error of the 12-m dish stated in the ALMA Project Book is $0.6''$. We consider rms pointing error of $0.6''$ as an ideal case and $1.2''$ to represent a poor pointing accuracy condition and tested all combinations of these two values of pointing errors among ALMA, ACAi and SD. The simulations with the same set of the parameters were ran 10 times to obtain averaged values of fidelities. While it is difficult to quote the uncertainties of the determined fidelity, the uncertainties estimated from the scatters in median fidelities (with 1% intensity threshold) among the 10 simulations are 5-10%.

Table 4 and 5 show the image fidelity medians with pixel intensity threshold of 1% at 230 and 850 GHz, respectively. The *fidelity gain*, a factor of the median fidelity improved by adding ACA, is given in the last columns. Figure 7 summarizes these tables for "all" case (ALMA+ACAi+SD). The influence of pointing errors is significant for 850 GHz cases as the fidelity gain quickly declined as the pointing errors increase. Even with a pointing error of $0.6''$, which is the current ALMA specification, at 850 GHz it corresponds to ∼9% and ∼5% of beams (FWHM) of the 12-m and 7-m antennas, respectively. As shown in Figure 7, when pointing errors of the 12-m antennas of ALMA (the 64-element array) and SD are $0.6''$ (green solid lines),pointing errors of ACA 7-m also significantly influence the image quality. However, in the case for a pointing error of the ALMA 12-m is $1.2''$, the pointing errors of ACA 7-m and SD 12-m do have a little influence and the fidelity is below 20 for most of the cases at 850 GHz. So for pointing errors, the errors of the 64-element array have most impact in imaging while the errors of ACA have less impact. However, to achieve high fidelity imaging at good conditions, the pointing accuracy specification of the ACA 7-m antenna should not be relaxed since it also contribute to degrading of the fidelity. Behavior of the fidelity also depends on the structure of the source model. The HCO43 model which has a relatively simple structure as shown in image and *uv* distribution in Figure 2, is showing greater improvement with ACA than other models.

| 230GHz | | | | | |

model	ALMA	ACA7m, SD	$ALMA+SD$	all	fidelity gain
		pointing error	median fidelity (intensity threshold 1%)		
HCO43		no err.	8	105	14.0
	0.6″	0.6″, 0.6″	8	87	11.3
		1.2″, 0.6″	8	72	9.5
		0.6″, 1.2″	8	68	8.6
		1.2″, 1.2″	8	65	8.2
	1.2″	0.6″, 0.6″	8	72	9.3
		1.2″, 0.6″	8	67	8.4
		0.6″, 1.2″	8	57	7.1
		1.2″, 1.2″	8	58	7.0
M51Hα		no err.	28	151	5.4
	0.6″	0.6″, 0.6″	29	111	3.9
		1.2″, 0.6″	28	106	3.8
		0.6″, 1.2″	32	97	3.0
		1.2″, 1.2″	32	93	2.9
	1.2″	0.6″, 0.6″	28	75	2.7
		1.2″, 0.6″	27	75	2.7
		0.6″, 1.2″	29	72	2.5
		1.2″, 1.2″	30	70	2.4
cluster		no err.	65	267	4.1
	0.6″	0.6″, 0.6″	60	168	2.8
		1.2″, 0.6″	63	137	2.2
		0.6″, 1.2″	49	133	2.7
		1.2″, 1.2″	53	136	2.6
	1.2″	0.6″, 0.6″	45	110	2.4
		1.2″, 0.6″	50	106	2.1
		0.6″, 1.2″	43	114	2.6
		1.2″, 1.2″	47	98	2.1
M31		no err.	99	220	2.2
	0.6″	0.6″, 0.6″	85	144	1.7
		1.2″, 0.6″	83	119	1.4
		0.6″, 1.2″	71	105	1.5
		1.2″, 1.2″	72	102	1.4
	1.2″	0.6″, 0.6″	68	109	1.6
		1.2″, 0.6″	66	99	1.5
		0.6″, 1.2″	59	98	1.7
		1.2″, 1.2″	59	90	1.5

Table 4: Image fidelity medians for different combinations of pointing errors at 230GHz.

| | | | median fidelity (intensity threshold 1%) | | |
model	ALMA	ACA7m, SD	$ALMA+SD$	all	fidelity gain
HCO43		no err.	8	105	14.0
	0.6″	0.6″, 0.6″	9	31	3.6
		1.2″, 0.6″	9	22	2.4
		0.6″, 1.2″	10	14	1.4
		1.2″, 1.2″	11	13	1.3
	1.2″	0.6″, 0.6″	10	22	2.3
		1.2″, 0.6″	10	19	1.8
		0.6″, 1.2″	13	12	0.9
		1.2″, 1.2″	13	13	1.0
M51Hα		no err.	29	156	5.4
	0.6″	0.6″, 0.6″	27	36	1.3
		1.2″, 0.6″	28	30	1.1
		0.6″, 1.2″	14	18	1.2
		1.2″, 1.2″	14	17	1.2
	1.2″	0.6″, 0.6″	12	14	1.2
		1.2″, 0.6″	12	14	1.2
		0.6″, 1.2″	11	13	1.1
		1.2″, 1.2″	11	13	1.1
cluster		no err.	63	255	4.1
	0.6″	0.6″, 0.6″	24	44	1.9
		1.2″, 0.6″	25	34	1.3
		0.6″, 1.2″	11	22	1.9
		1.2″, 1.2″	12	16	1.4
	1.2″	0.6″, 0.6″	12	18	1.5
		1.2″, 0.6″	12	18	1.5
		0.6″, 1.2″	9	17	1.9
		1.2″, 1.2″	9	15	1.7
M31		no err.	99	222	2.2
	0.6″	0.6″, 0.6″	26	35	1.3
		1.2″, 0.6″	26	24	0.9
		0.6″, 1.2″	11	16	1.5
		1.2″, 1.2″	11	14	1.3
	1.2″	0.6″, 0.6″	12	16	1.4
		1.2″, 0.6”	12	15	1.2
		0.6″, 1.2″	9	12	1.3
		1.2″, 1.2″	9	13	1.4

Table 5: Same as Table 4 but at 850GHz.

15
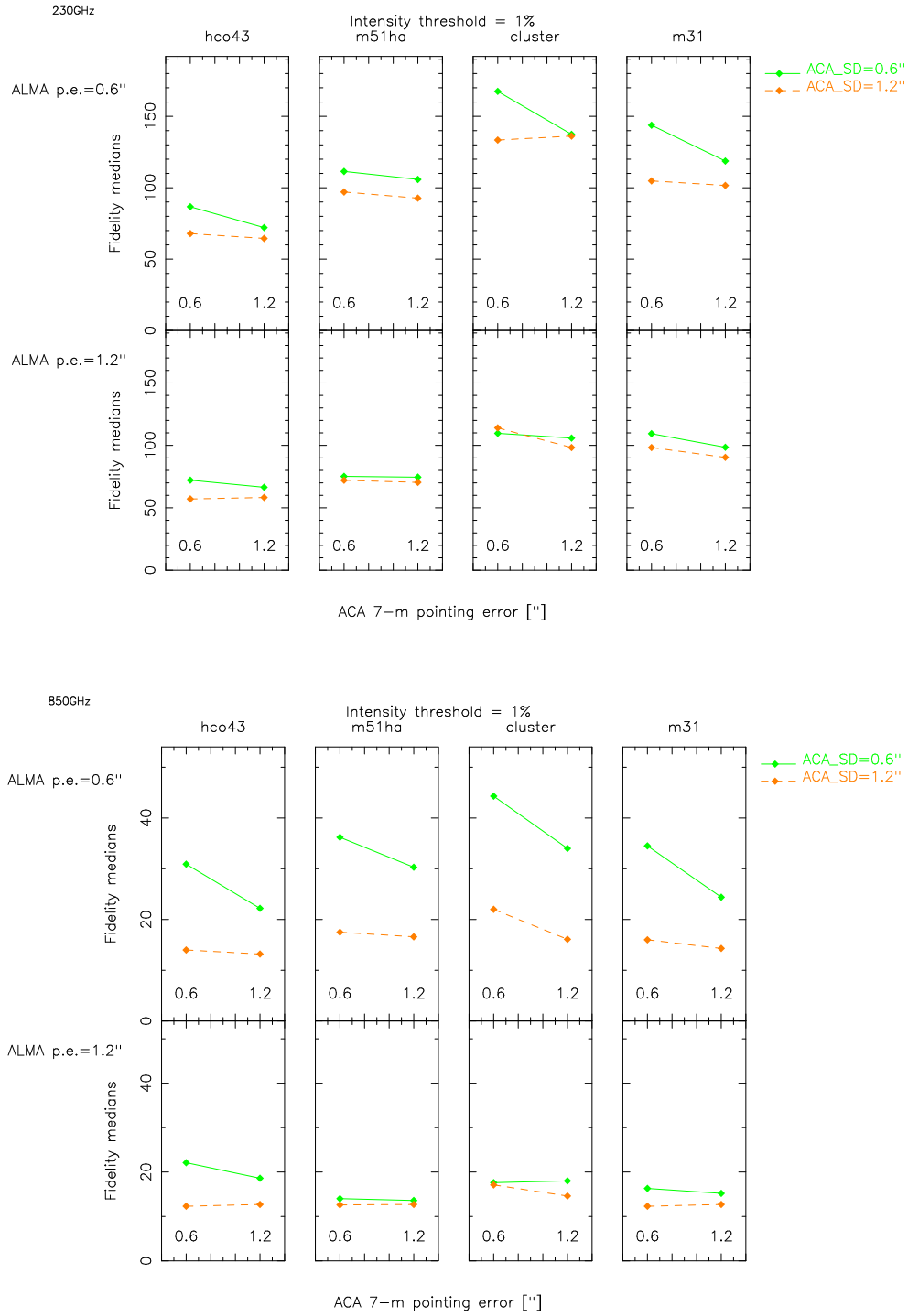
Figure 7: Image fidelity medians as a function of the ACA-7m pointing errors in presence of the ALMA pointing error of $0.6''$(*upper panel*) and of $1.2''$(*lower panel*) at 230 (*top*) and 850 GHz (*bottom*). The green solid line: for the ACA-12m single dish pointing error of $0.6''$; the orange dashed line: for the ACA 12-m pointing error of $1.2''$.

16

4.2 Amplitude Gain Errors

Amplitude gain errors are simulated by considering two terms: offset which is constant in time, and drift which varies with time. Main sources of amplitude gain error are variations of atmospheric transmission, antenna gain variations caused by defocus and dish distortion, and receiver gain fluctuation and drift. Both terms are considered to be random residual errors after amplitude calibration done every 15 minutes. The values were reset randomly for each antennas. Equal rms values of amplitude errors were entered on each of the 64-element and ACA arrays, and SD. At 230 GHz, slow variation of antenna gain and receiver gain drift are assumed to be negligible and thus no drift term is considered. At 850 GHz, we assume that the two terms have equal weight.

Degradation of the fidelity with amplitude gain errors of 0, 1, 3, and 10% rms at 230 GHz is shown in Table 6 and Figure 8. Each fidelity is an averaged value of 10 simulations performed with the same set of parameters. For all the models, amplitude gain errors of 3% result in degradation of the fidelity by a roughly factor of two. In Figure 9, the case of offset amplitude errors at 850 GHz is shown. The trend is similar to those at 230 GHz but slightly stronger effect as the errors increase. The drift term has less effect on fidelity as shown in Figure 10. It is shown that if the amplitude gain errors are at the ALMA specification, 1% and 3% or less at 230 and 850 GHz, respectively, the fidelity improves by factor of two or greater for most of the cases by adding ACAi. While the fidelity for ALMA+ACAi+SD is generally a smooth function of amplitude gain errors, for ALMA+SD, it occasionally show spurious values that are higher than those in the absence of error as seen in M31 and cluster cases. These effects could partly be caused when the deconvolution fails for part of an image in the absence of error (Pety et al. 2001c).

230GHz				
model	amplitude gain error [%]	median fidelity (Intensity threshold 1%) $ALMA+SD$	all	$fidelity\ gain$
HCO43	0	8	105	14.0
	1	8	89	11.9
	3	8	53	7.0
	10	7	22	3.1
M51Hα	0	28	151	5.4
	1	29	105	3.7
	3	28	79	2.9
	10	26	32	1.2
cluster	0	65	267	4.1
	1	63	213	3.4
	3	64	91	1.4
	10	58	47	0.8
M31	0	99	220	2.2
	1	106	177	1.7
	3	122	134	1.1
	10	75	52	0.7

Table 6: Image fidelity medians at 230GHz as a function of amplitude gain errors. The amplitude gain errors here are modelled as random offsets.

850GHz	offset term only			
	amplitude gain error [%]	median fidelity (Intensity threshold 1%)		
model		$ALMA+SD$	all	fidelity gain
HCO43	0	8	105	14.0
	3	8	79	10.5
	10	7	28	3.8
M51Hα	0	29	156	5.4
	3	29	88	3.1
	10	29	28	1.0
cluster	0	63	255	4.1
	3	62	94	1.5
	10	49	62	1.3
M31	0	99	222	2.2
	3	103	104	1.0
	10	56	58	1.1

Table 7: Image fidelity medians at 850GHz as a function of amplitude gain errors given by (time-independent) random offsets.

850GHz	drift term only			
	amplitude gain error [%]	median fidelity (Intensity threshold 1%)		
model		$ALMA+SD$	all	fidelity gain
HCO43	0	8	105	14.0
	3	8	92	12.1
	10	8	55	6.9
M51Hα	0	29	156	5.4
	3	28	143	5.2
	10	25	89	3.5
cluster	0	63	255	4.1
	3	83	213	2.6
	10	80	103	1.3
M31	0	99	222	2.2
	3	135	177	1.3
	10	174	99	0.6

Table 8: Image fidelity medians at 850GHz as a function of amplitude gain errors given by time dependent drift term.
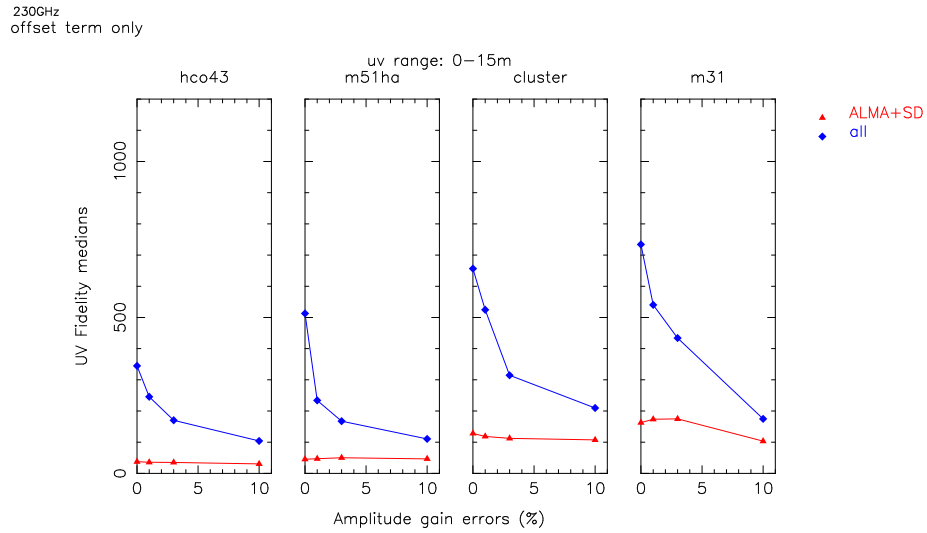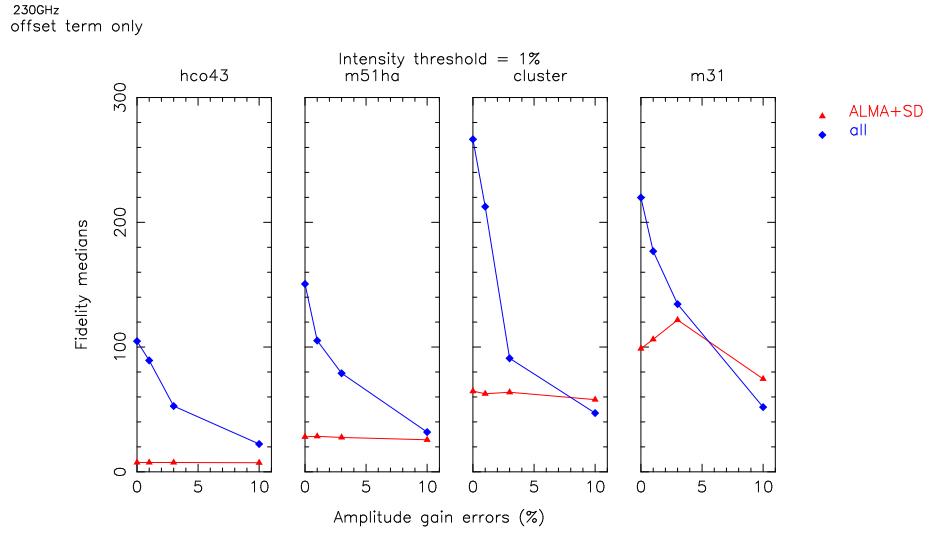
Figure 8: Degradation of fidelity by amplitude gain errors considering offset term only at 230 GHz. *upper panel:* Image fidelity medians as a function of amplitude gain errors in percent. *lower panel: uv*-domain fidelity in the *uv* range of 0-15m. The red lines: ALMA+SD; the blue lines: ALMA+ACAi+SD by the hybrid method.
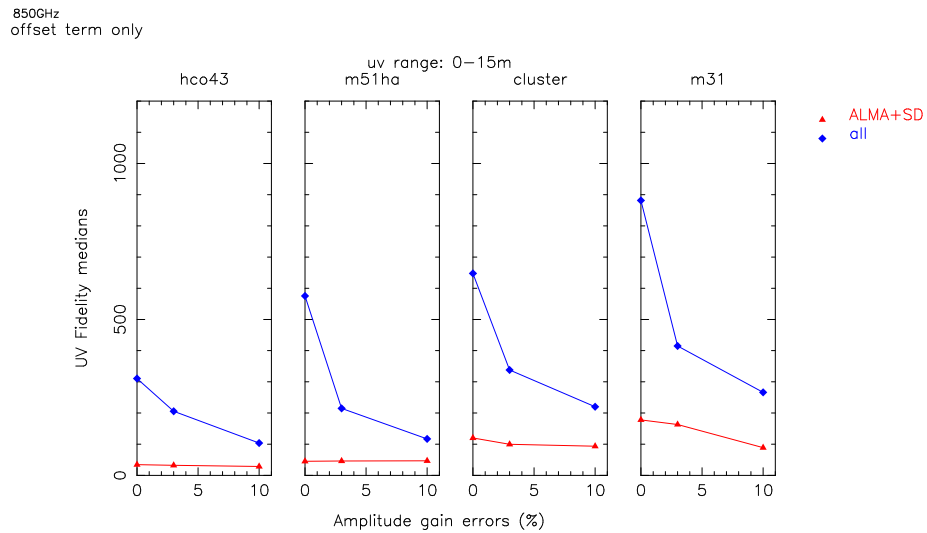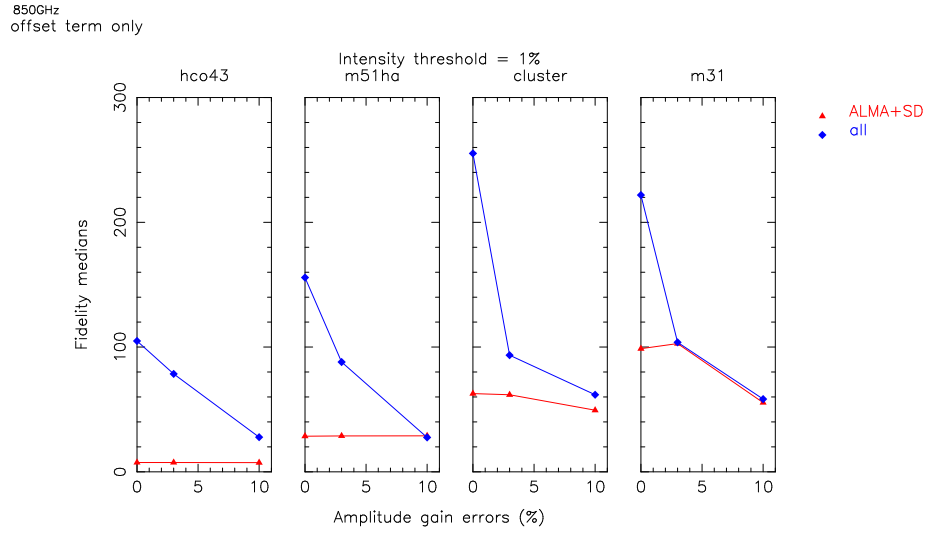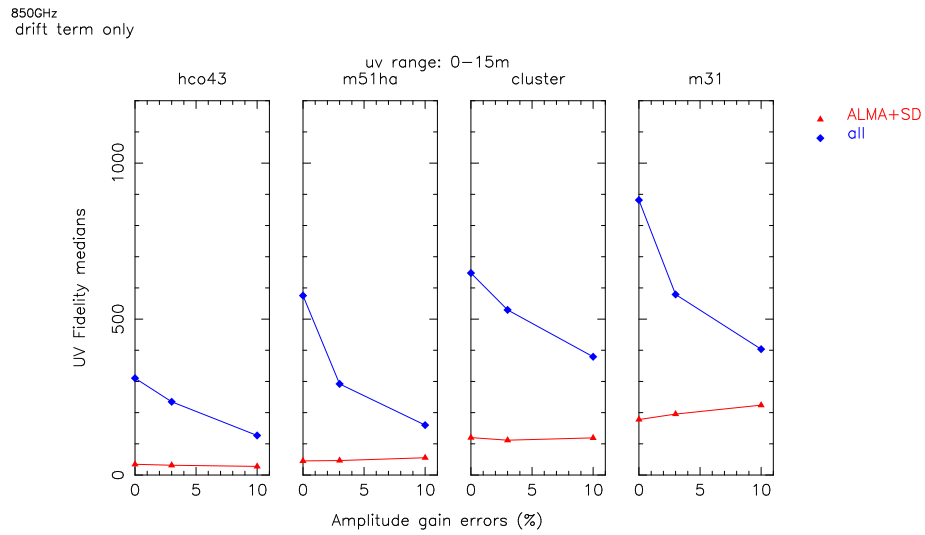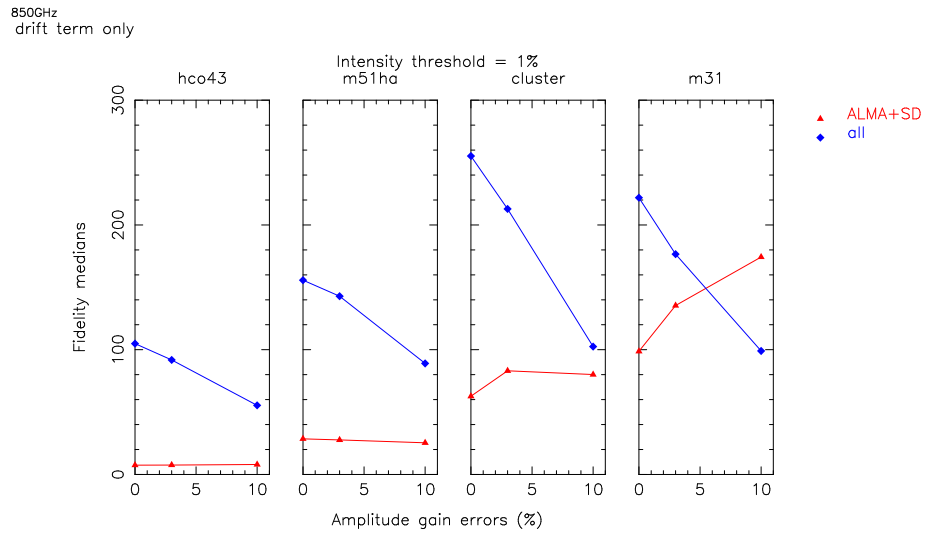
Figure 9: Degradation of fidelity by amplitude gain errors considering offset term only at 850 GHz. *upper panel:* Image fidelity medians as a function of amplitude gain errors in percent. *lower panel: uv*-domain fidelity in the *uv* range of 0-15m. The red lines: ALMA+SD; the blue lines: ALMA+ACAi+SD by the hybrid method.

Figure 10: Same as Figure 8 but considering drift term only at 850 GHz. *upper panel:* Image fidelity medians as a function of amplitude gain errors in percent. *lower panel: uv*-domain fidelity in the *uv* range of 0-15m. The red lines: ALMA+SD; the blue lines: ALMA+ACAi+SD by hybrid method.

4.3 Atmospheric Phase Errors

Atmospheric phase errors are simulated using a 2-D phase screen model generated with a 2nd order structure function. For our simulations, we assumed that the power of the 2nd order structure function to be 0.61, wind velocity of 10m/s at altitude of 1000m. The angular separation between a calibrator and a target source were taken to be 2 degrees. The standard calibration is employed by intervening the calibrator and target source (2sec on the calibrator and 20sec on the target) in 26-second cycles. Calibration by water vapor radiometry (WVR) is also applied. Due to the current design of the simulator, these calibrations are applied to both the 64-element and ACA arrays. For ACA, these calibration schemes do not help to improve imaging quality and even add some noises introduced by calibration errors. The fast switching method does not work for ACA since all the ACA baselines are much less than 100m and the phase pattern passes by above the array in less time than the fast switching cycle. The current WVR is not sensitive enough to correct phase degradation for the ACA baselines. For the baselines less than 60m, there is a little difference in phase noises between after applying different calibration methods (WVR calibration, fast switching, or combination of both) and without any calibration as shown in Figure 3 of Pety et al (2001c). In test simulations that we ran for the cases with no phase calibration at all, uv fidelities of ALMA+ACAi+SD in the 0-15m range actually improved sometimes by a factor of two for the case with both fast switching and wvr calibrations being applied.

The simulations were performed by varying the phase noise of the phase screen model with the fixed power. Table 9 lists the simulation results in terms of phase conditions in percentile at 230 and 850 GHz determined from the site data at Chajnantor (Holdaway 2003, private communication). The set of percentiles represents good and poor (but still doable) observing conditions at millimeter and submillimeter wavelengths. Image fidelity and uv-plane fidelity as a function of phase noise at 100m are plotted in Figure 11. For "good" phase conditions (25% and 5% for 230 and 850 GHz, respectively), the fidelity improved by a factor of two or more by adding ACA except M31 model. For the case of "poor" conditions, the improvement is limited. Since the phase calibrations of ACAi data may in fact lead to degrading of fidelity, these results should be considered to be lower limits.

model	site condition		median fidelity (intensity threshold 1%)		
	230GHz	850GHz	$ALMA + SD$	all	$fidelity\ gain$
HCO43	0% (no err.)		8	105	14.0
	25%	5%	8	67	8.6
	50%	10%	8	39	4.8
M51Hα	0% (no err.)		28	151	5.4
	25%	5%	24	57	2.3
	50%	10%	18	28	1.5
cluster	0% (no err.)		65	267	4.1
	25%	5%	52	97	1.9
	50%	10%	37	50	1.3
M31	0%(no err.)		99	220	2.2
	25%	5%	66	84	1.3
	50%	10%	41	41	1.0

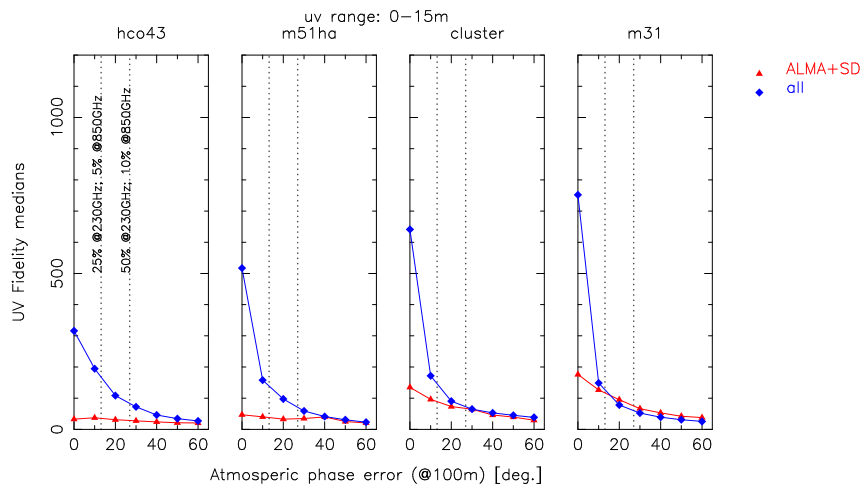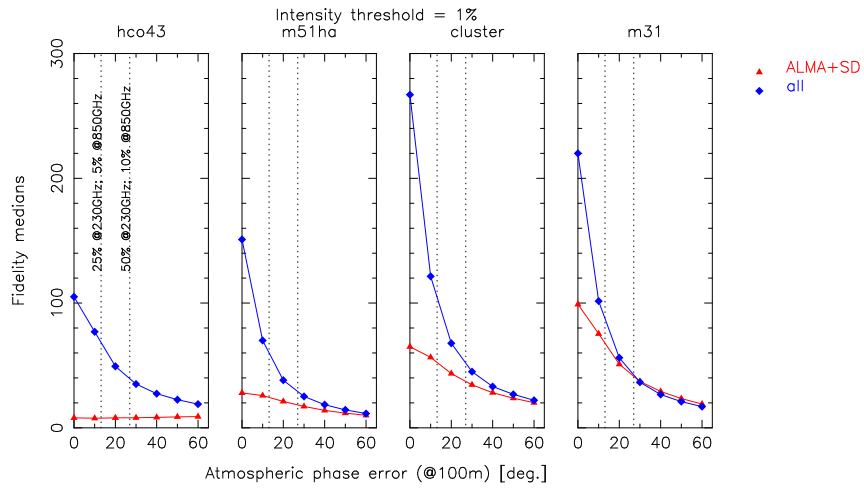Table 9: Image fidelity medians as a function of atmospheric condition at the site given in percentiles.

Figure 11: *upper panel:* Image fidelity medians as a function of atmosheric phase error (rms) at 100-m baseline. *lower panel:* *uv*-domain fidelity medians in *uv* range of 0-15m. The red lines: ALMA+SD; the blue lines: ALMA+ACA+SD by hybrid method. The dashed lines indicate 25% (at 230 GHz) or 5% (at 850 GHz), and 50% (230 GHz) or 10% (850 GHz)

4.4 Simulations Including All the Errors

In the previous sections, we simulated by selecting one component of errors at a time. To reflect more realistic situations, we also performed the simulations including all the errors. To represent typical observing conditions, the parameters were chosen based on the ALMA specifications, which are $0.6''$ rms for pointing errors, 1% (offset term) at 230 GHz and 3% (offset and drift terms combined) at 850 GHz for amplitude errors. The simulations were ran for the two cases of atmospheric condition as in Section 4.3.

Figure 12 and 13 show the image and *uv* fidelities (averaged values of 10 simulations with identical parameters) in terms of the atmospheric condition. The fidelities that are free of any errors are plotted as 0% of the atmospheric condition. As similar to what Pety et al (2001) found in their simulations including all typical errors, the general trend is that introduction of errors greatly reduces the fidelity and its variation among the four tested models are less significant than the error free case. For HCO43 model, the rate of degrading is less as compared with the other models at both frequencies. The sharper drops in fidelity for 850-GHz case (from error free case to 5-percentile) than 230-GHz case are mainly caused by a larger fraction of pointing errors with respect to the beams. The relative contribution of ACA can be seen better in terms of the fidelity gain ($\frac{all}{ALMA+SD}$) listed in Table 10 and 11. For the HCO43 model, a factor of two or better improvement is seen by the inclusion of ACA under good and poor observing conditions at both frequencies. For the M51Hα and cluster models, some improvements are seen at good observing conditions. In the case of M31, the contribution of ACA is much less even at best observing conditions at these particular frequencies.
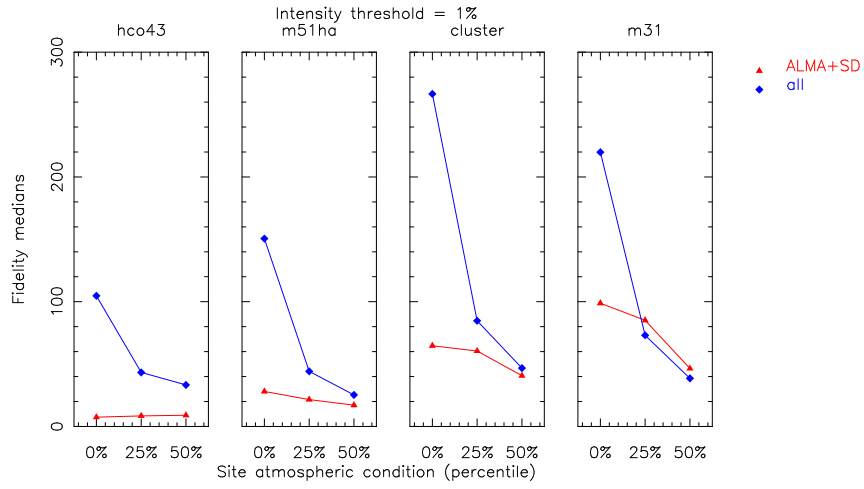
230GHz				
model	site condition	median fidelity (intensity threshold 1%)		
		$ALMA+SD$	all	$fidelity\ gain$
HCO43	0% (no err.)	8	105	14.0
	25%	9	43	5.1
	50%	9	33	3.7
M51Hα	0% (no err.)	28	151	5.4
	25%	22	44	2.0
	50%	17	25	1.5
cluster	0% (no err.)	65	267	4.1
	25%	61	85	1.4
	50%	41	47	1.1
M31	0% (no err.)	99	220	2.2
	25%	85	73	0.9
	50%	47	39	0.8

Table 10: Image fidelity medians at intensity threshold of 1% and "fidelity gain" ($\frac{all}{ALMA+SD}$) at 230GHz.

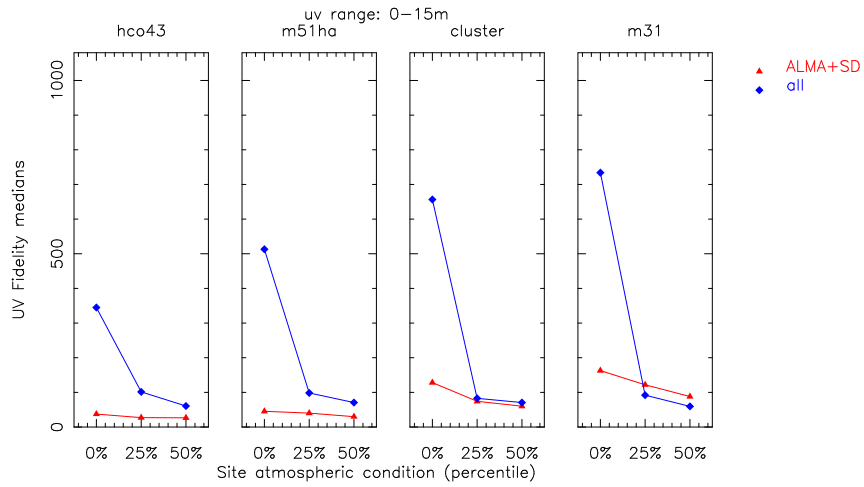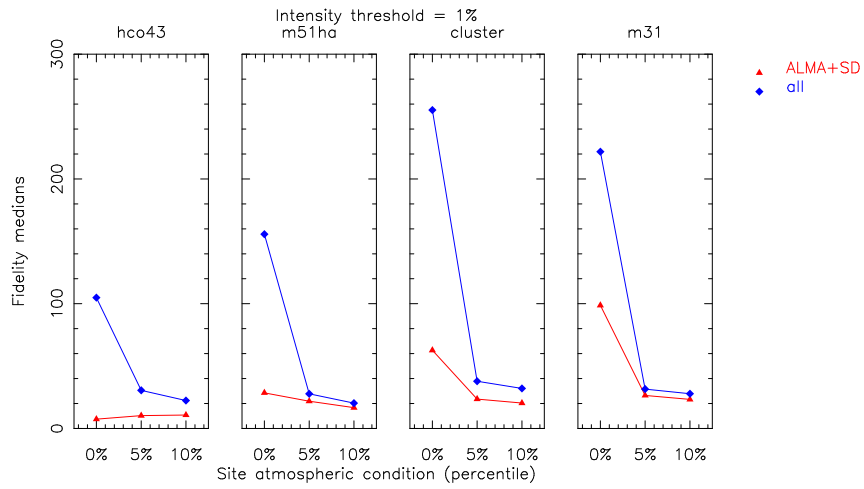| 850GHz				
model	site condition	median fidelity (intensity threshold 1%)		
		$ALMA+SD$	all	$fidelity\ gain$
HCO43	0% (no err.)	8	105	14.0
	5%	10	31	3.0
	10%	11	22	2.1
M51Hα	0% (no err.)	29	156	5.4
	5%	22	28	1.3
	10%	17	20	1.2
cluster	0% (no err.)	63	255	4.1
	5%	24	38	1.6
	10%	20	32	1.6
M31	0% (no err.)	99	222	2.2
	5%	27	32	1.2
	10%	23	28	1.2

Table 11: Same as Table 10 but at 850GHz

Figure 12: 230 GHz fidelity versus the atmospheric condition. *upper panel:* Image fidelity medians including all the errors. *lower panel:* *uv*-domain fidelity medians in *uv* range of 0-15m. The red lines: ALMA+SD; the blue lines: ALMA+ACA+SD by the hybrid method
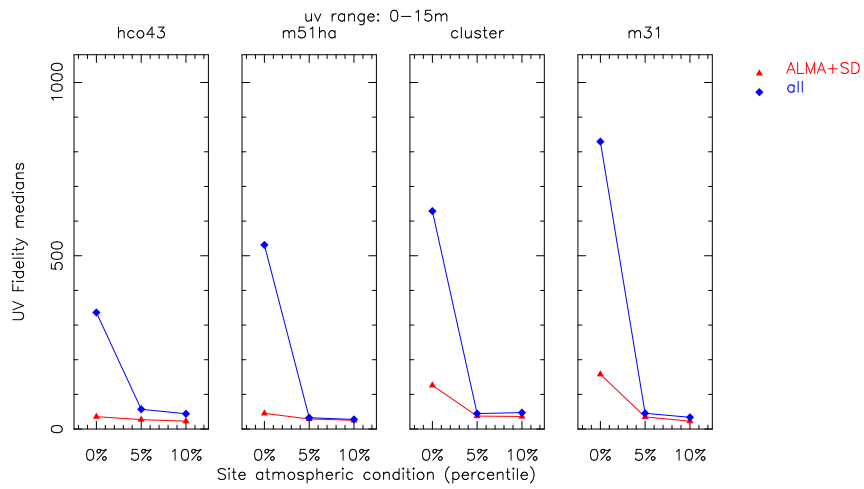
Figure 13: 850 GHz fidelity versus the atmospheric condition. *upper panel:* Image fidelity medians including all the errors. *lower panel:* *uv*-domain fidelity medians in *uv* range of 0-15m. The red lines: ALMA+SD; the blue lines: ALMA+ACA+SD by the hybrid method

4.5　Summary of Sec. 4

We examined relative contribution of each component of pointing, amplitude gain, and atmospheric phase errors in degrading the image quality in the ALMA 64-element array+ACA system.

- At 230 GHz, relative contributions of pointing and amplitude gain errors in image quality are about the same. Having pointing errors of $0.6''$ (or $1.2''$) results in similar fidelity as the case of having amplitude gain errors of 1% (or 3%). In such cases, atmospheric phase errors are the dominant factor.

- At 850 GHz, pointing errors have the dominant effect followed by atmospheric phase errors. The effect of amplitude gain errors is relatively small as long as these errors remain near the ALMA specification.

- For the simulations with atmospheric phase errors, fidelity of data including ACA could be improved by different calibration scheme or applying no calibration at all while in the current scheme the calibration method is globally set for both ALMA and ACA arrays.

For significant influence of atmospheric phase errors at the both frequencies indicated by these simulations, the calibration by fast switching or WVR are ineffective in the current specifications of these techniques. The calibration methods specific to ACA remain to be a subject for studies.

In addition to the last point described above, the array configuration combination used here (C1 for ALMA and a spiral for ACA) probably gives a lower limit of the fidelity gain produced by the ACA system as we stated in the Section 3.

The science requirements in the Project Description of Atacama Compact Array System states that ALMA 64-element array with the ACA system should routinely achieve a median fidelity >20 in average observing condition at $\nu <345$ GHz, and the similar level of fidelity in favorable condition at $\nu >345$ GHz. Our simulations support that these requirements are reasonably met providing that both the 64-element array and ACA system comply with their specifications.

5　Conclusions and Future Works

In summary:

1 **From the simulations with different ACA array characteristics, we found that an array densely packed toward the center generally gives good imaging performance. The antenna close packing ratio of 1.25 in the ALMA specification should also apply to ACA.**

2 **For the simulations with a variety of errors assumed, the atmospheric phase errors are a dominant factor at millimeter wavelengths in limiting the quality of the wide-field imaging with ALMA including the ACA system. The effects of the pointing errors and amplitude gain errors have similar, but secondary, contribution. At submillimeter wavelengths, the effect of the pointing errors become dominant factor to limit the imaging quality with the atmospheric phase errors being second.**

3 **To maximize the merit of ACA in the wide-field imaging capability of ALMA, accurate pointing of the ACA 7-m antenna is important. The absolute value of pointing errors should be as good as that of the 12-m antenna of the 64-element array.**

There are other parameters to be explored in simulations that is left to future works. The following is a list of such items.

- Simulations at different source declinations to study shadowing effect. In the current simulations, the durations of observations in our simulations were short and the observations were assumed to be made near zenith, and the effect of shadowing were not explored.

- Simulations with sparser 64-element array configurations are needed since in the current simulations we combined ACA only with the most compact configuration of the 64-element array (C1).

- For more thorough imaging study in the presence of pointing errors, one should also include effect of dynamic refraction which is not included in the present simulations.

- The effects of instrumental phase errors are not included in the present simulations. To do that one needs to generate some error models which reflect the sources of the errors.

- Simulations including thermal noise. Morita (2001) performed the imaging simulations including thermal noise using the MEM. It would be interesting to compare if there is any difference by the deconvolution method used.

References

Boone, F. 2001, "Interferometric array design: Optimizing the locations of the antenna pads", A&A, 377 , 368.

Cornwell, T.J., Holdaway, M.A., and Uson, J.M. 1993, "Radio-interferometric imaging of very large objects: implications for array design", A&A, 271, 687.

Holdaway, M. 1997, ALMA Memo 178, "Effects of Pointing Errors on Mosaic Images with 8m, 12m, and 15m Dishes"

Morita, K.-I. 2001, ALMA Memo 374, "Wide Field Imagings with the Atacama Large Millimeter/Submillimeter Array"

Morita, K.-I, and Holdaway, M. A. 2004, ALMA Memo in preparation.

Pety, J., Gueth, F., and Guilloteau, S. 2001a, ALMA Memo 396, "ALMA+ACA Simulation Tool"

Pety, J., Gueth, F., and Guilloteau, S. 2001b, ALMA Memo 397, "ALMA+ACA Simulation Results"

Pety, J., Gueth, F., and Guilloteau, S. 2001c, ALMA Memo 398, "Impact of ACA on the Wide-Field Imaging Capabilities of ALMA"

van Dishoeck E.F., Wootten, A., and Guilloteau, S. 2003, "The ALMA Design Reference Science Plan Version 1.0" (http://www.strw.leidenuniv.nl/ joergens/alma/)

Wright, M.C.H. 2003, ALMA Memo 450, "Heterogeneous Imaging with the ALMA Compact Array"

Yun, M. S. 2001, ALMA Memo 368, "An Imaging Study for ACA"